Dipole tilt effects on the magnetosphere-ionosphere convection system during interplanetary magnetic field B_Y-dominated periods: MHD modeling

Masakazu Watanabe,[1] Konstantin Kabin,[2] George J. Sofko,[3] Robert Rankin,[2] Tamas I. Gombosi,[4] and Aaron J. Ridley[4]

Received 17 September 2009; revised 8 December 2009; accepted 14 January 2010; published 21 July 2010.

[1] Using numerical magnetohydrodynamic simulations, we examine the dipole tilt effects on the magnetosphere-ionosphere convection system when the interplanetary magnetic field is oblique northward (B_Y = 4 nT and B_Z = 2 nT). In particular, we clarify the relationship between viscous-driven convection and reconnection-driven convection. The azimuthal locations of the two viscous cell centers in the equatorial plane rotate eastward (westward) when the dipole tilt increases as the Northern Hemisphere turns toward (away from) the Sun. This rotation is associated with nearly the same amount of eastward (westward) rotation of the equatorial crossing point of the dayside separator. The reason for this association is that the viscous cell is spatially confined within the Dungey-type merging cell whose position is controlled by the separator location. The ionospheric convection is basically a round/crescent cell pattern, but the round cell in the winter hemisphere is significantly deformed. Between its central lobe cell portion and its outer Dungey-type merging cell portion, the round cell streamlines are deformed owing to the combined effects of the viscous cell and the hybrid merging cell, the latter of which is driven by both Dungey-type reconnection and lobe-closed reconnection.

Citation: Watanabe, M., K. Kabin, G. J. Sofko, R. Rankin, T. I. Gombosi, and A. J. Ridley (2010), Dipole tilt effects on the magnetosphere-ionosphere convection system during interplanetary magnetic field B_Y-dominated periods: MHD modeling, *J. Geophys. Res.*, *115*, A07218, doi:10.1029/2009JA014910.

1. Introduction

[2] Knowledge of plasma convection is fundamental to the understanding of the magnetosphere-ionosphere system [*Tanaka*, 2007]. On a global scale, the plasma velocity and the magnetic field are the basic parameters that describe the plasma dynamics [*Parker*, 1996; *Vasyliūnas*, 2001, 2005a, 2005b]. The concept of convection in the magnetosphere-ionosphere system started with two pioneering works, both of which, by a curious coincidence, were published in 1961. *Dungey* [1961] suggested that for due southward interplanetary magnetic field (IMF), IMF to closed reconnection on the dayside and north lobe (NL) to south lobe (SL) reconnection on the nightside drive a plasma circulation mode which appears as two-cell convection in the ionosphere (the so-called Dungey cycle). *Axford and Hines* [1961] suggested that the viscous-like interaction between the solar wind and the magnetospheric plasma in the low-latitude boundary layer excites morningside and afternoonside vortices in the closed field line region. A decade later, *Russell* [1972] proposed that IMF-NL reconnection or IMF-SL reconnection produces plasma circulation that is confined to the open field line region. These three circulation modes form the classic framework of steady state convection in the magnetosphere-ionosphere system [*Reiff and Burch*, 1985]. In the ionosphere, the convection cells resulting from the three circulation modes are called the merging cell (which crosses the polar cap boundary twice in one cycle), the viscous cell (which circulates outside the polar cap), and the lobe cell (which circulates inside the polar cap). Here, the polar cap is the open field line region in the ionosphere, and we call its equatorward edge (i.e., the open-closed field line boundary) the polar cap boundary.

[3] For reconnection-driven convection, there have been significant advances since the *Reiff and Burch* [1985] paper. For due northward IMF and significant dipole tilt, *Crooker* [1992] suggested a plasma circulation mode which may be called the "reverse" Dungey cycle. Analogous to the "normal" Dungey cycle, the reverse Dungey cycle proceeds from IMF-closed reconnection at high latitudes in one hemisphere followed by NL-SL reconnection at high latitudes in the opposite hemisphere. As a result, a pair of

[1]Department of Earth and Planetary Sciences, Graduate School of Sciences, Kyushu University, Fukuoka, Japan.
[2]Department of Physics, University of Alberta, Edmonton, Alberta, Canada.
[3]Department of Physics and Engineering Physics, University of Saskatchewan, Saskatoon, Saskatchewan, Canada.
[4]Department of Atmospheric, Oceanic, and Space Sciences, University of Michigan, Ann Arbor, Michigan, USA.

0148-0227/10/2009JA014910

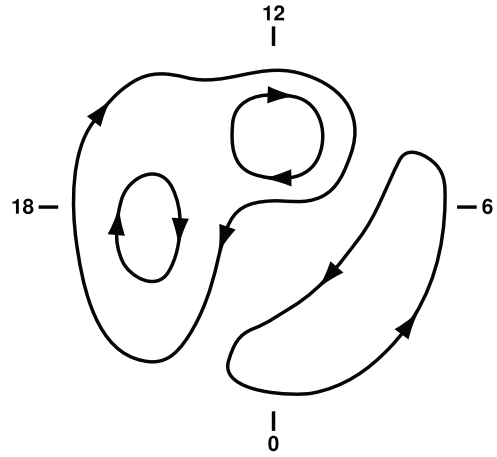

Figure 1. An uncommon convection pattern in the Northern Hemisphere seen near the December solstice for IMF $B_Y > B_Z > 0$.

reverse merging cells whose circulation directions are opposite to those of the normal Dungey cycle appears in the ionosphere in both hemispheres. Later, *Tanaka* [1999], on the basis of magnetohydrodynamic (MHD) simulation, suggested a new type of reconnection which occurs between lobe field lines and closed field lines. Following this suggestion, some new plasma circulation modes were found in association with lobe-closed reconnection. The circulation mode is parameterized by the IMF clock angle $\theta_c \equiv \mathrm{Arg}(B_z + iB_y)$, where $\mathrm{Arg}(z)$ is the function that returns the argument of a complex number z in the interval $-180° < \mathrm{Arg}(z) \leq 180°$. When the IMF is nearly due northward ($|\theta_c| \lesssim 30°$), lobe-closed reconnection and IMF-lobe reconnection form the "interchange cycle" which produces in the ionosphere a "reciprocal cell" in one hemisphere and an "interchange-type merging cell" in the other hemisphere [*Watanabe et al.*, 2005; *Watanabe and Sofko*, 2009a, 2009b]. The reciprocal cell circulates exclusively in the closed field line region, but its circulation direction is opposite to that of the viscous cell. When the IMF B_Y component is dominant ($120° \gtrsim |\theta_c| \gtrsim 30°$), lobe-closed reconnection and Dungey-type reconnection form the "hybrid cycle" which produces in the ionosphere a variety of "hybrid merging cells" in both hemispheres [*Watanabe et al.*, 2004, 2007; *Watanabe and Sofko*, 2008].

[4] When the IMF B_Y component is dominant ($120° \gtrsim |\theta_c| \gtrsim 30°$), ionospheric convection exhibits a distorted two-cell pattern with its dawn-dusk and interhemispheric asymmetries regulated by the IMF B_Y polarity. For IMF $B_Y > 0$ ($B_Y < 0$), in the northern ionosphere, the dawnside (duskside) cell is crescent-shaped, while the duskside (dawnside) cell is relatively round and extends to the dawnside (duskside) ionosphere beyond the noon meridian; the pattern in the southern ionosphere is basically a mirror image of the northern ionosphere with respect to the noon-midnight meridian [e.g., *Burch et al.*, 1985; *Lu et al.*, 1994]. In this paper, we use the terms "round cell" and "crescent cell" to describe the IMF B_Y-regulated convection cells. In the classic framework of *Reiff and Burch* [1985], the round cell consists of a merging cell and a lobe cell, while the crescent cell consists of a merging cell and a viscous cell. In the reconnection-based modern view of *Watanabe et al.* [2007] and *Watanabe and Sofko* [2008, 2009a], the round cell consists of a lobe cell, a Dungey-type merging cell, and a hybrid merging cell, whereas the crescent cell is a pure Dungey-type merging cell. Note that in both the classic and modern pictures, the round cell does not include a viscous cell.

[5] In the modern picture, the round cell is a consequence of four types of reconnection, namely, IMF-closed, IMF-lobe, lobe-lobe, and lobe-closed. When the X lines of the four types of reconnection are projected to the ionosphere in the same hemisphere as the null point, they are anchored to the foot point of the "stemline" [*Siscoe et al.*, 2001b] which connects the magnetic null and the ionosphere (we call this point the topological cusp). Because of this spatial constraint on the projected X lines, the convection pattern in this hemisphere is a structurally stable round cell. Observations also support the stability of the round cell, because the round cell pattern is almost always observed during IMF B_Y-dominated periods. However, the authors of this paper, who have been analyzing Super Dual Auroral Radar Network (SuperDARN) data, have recently found several exceptional examples as sketched in Figure 1. This is a convection pattern observed in the Northern Hemisphere for IMF $B_Y > B_Z > 0$. Although it still holds the basic round/crescent cell structure, in this case the round cell on the duskside transforms into double cells. Since these examples were found exclusively around the December solstice, it was suspected that the transformation was due to dipole tilt effects. Motivated by this expectation, we investigate in this paper the dipole tilt effects on the magnetosphere-ionosphere convection system by means of numerical MHD simulation. Our aim is to provide a useful guide for interpreting observational data. A detailed comparison between observations and simulations will be submitted in future studies.

2. Outlook

[6] In magnetospheric studies, two coordinate systems are usually used: the Geocentric Solar Magnetospheric (GSM) coordinate system and the Solar Magnetic (SM) coordinate system [e.g., *Kivelson and Russell*, 1995, Appendix 3]. The Earth's dipole axis is parallel to the SM Z axis. When the dipole is tilted, the GSM Z axis and the SM Z axis are not parallel. We define the dipole tilt angle D as the signed angle between the GSM Z axis and the SM Z axis and positive for boreal summer. The value of D approximately ranges from −35° around 0500 UT on the December solstice to +35° around 1700 UT on the June solstice. In this paper, we use the GSM coordinates exclusively for presenting the simulation results.

[7] We examine the effect of dipole tilt on the magnetosphere-ionosphere convection system during IMF B_Y-dominated periods by using the BATS-R-US MHD simulation code [*Powell et al.*, 1999]. For this purpose, we performed three simulation runs for which the IMF and solar wind conditions remained the same but the dipole tilt angle changed as follows: (1) $D = 0°$, (2) $D = -20°$, and (3) $D = -35°$. For all three runs, the IMF parameters were set as $B_X = 0$ nT, $B_Y = 4$ nT, and $B_Z = 2$ nT ($\theta_c = 63°$), and the solar wind parameters were set as $v = 400$ km/s (speed), $\rho = 5$ amu/cc (mass density), and $T = 50{,}000$ K (temperature). In order to exclude ionospheric conductance effects, we assumed uni-

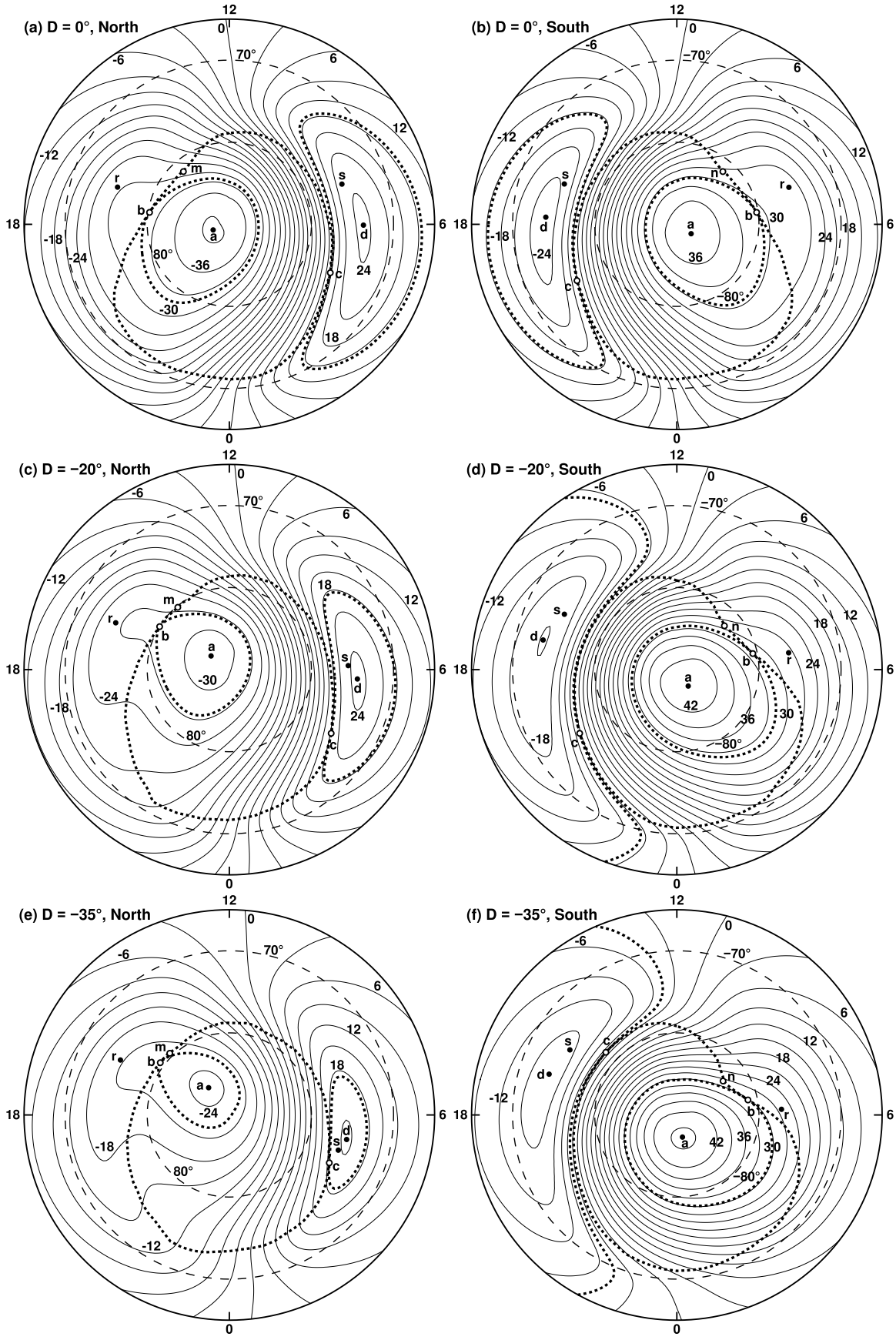
(a) D = 0°, North
(b) D = 0°, South
(c) D = −20°, North
(d) D = −20°, South
(e) D = −35°, North
(f) D = −35°, South
12
0
6
18
-6
70°
-70°
-12
-18
-24
-30
-36
80°
-80°
24
30
36
42
a
b
c
d
m
n
r
s

Figure 2

form ionospheric conductances, namely Σ_P = 1 S (Pedersen conductance) and Σ_H = 0 S (Hall conductance), for both hemispheres. The latter condition was deliberately chosen in order to exclude the dawn-dusk asymmetry which arises when there is a finite Hall conductance [*Ridley et al.*, 2004].

[8] Figure 2 shows ionospheric potentials for the three simulation runs, with Figures 2a, 2c, and 2e showing the Northern Hemisphere and Figures 2b, 2d, and 2f showing the Southern Hemisphere. Potential contours (Figure 2, solid lines) are shown every 3 kV and labeled every 6 kV. Figure 2 indicates that, for all the six cases, the potential contours exhibit the basic round/crescent cell pattern. Point a (point d) indicates the center of the round (crescent) cell. The large dotted loop encircling the polar region represents the polar cap boundary. Since point a (point d) is located far poleward (equatorward) of the polar cap boundary, the round (crescent) cell includes a substantial lobe (viscous) cell at its center. Point m (point n) on the polar cap boundary is the topological cusp in the Northern (Southern) Hemisphere. As the magnitude of the dipole tilt increases, the polar cap in the summer hemisphere becomes heart-shaped owing to the poleward deformation near the topological cusp (Figures 2d and 2f). This polar cap shape is consistent with that for the due northward IMF case [*Crooker*, 1992, Figure 3; *Watanabe et al.*, 2005, Figure 2]. Point b (point c) in Figure 2 indicates the location of the potential peak on the round-cell-side (crescent-cell-side) polar cap boundary. The dotted line that passes point b (point c) and lies poleward (equatorward) of the polar cap boundary is the potential contour that demarcates the boundary between the lobe (viscous) cell and the merging cell.

[9] We here introduce two new terms for the following discussion. For the $B_Y > 0$ case, on the duskside, the round (crescent) cell appears in the Northern (Southern) Hemisphere. Conversely, on the dawnside, the round (crescent) cell appears in the Southern (Northern) Hemisphere. In this paper, we examine the "conjugate" round and crescent cells on the duskside or dawnside. In order to deal with the duskside and dawnside convection systems synthetically, we use the terms "round cell hemisphere" and "crescent cell hemisphere." For the $B_Y > 0$ case, on the duskside (dawnside), the round cell hemisphere means the Northern (Southern) Hemisphere, whereas the crescent cell hemisphere means the Southern (Northern) Hemisphere.

[10] The convection pattern revealed by the simulation (Figure 2) poses two questions. First, when the dipole is tilted significantly, the round cell in the winter hemisphere is not really round but tadpole-shaped (Figures 2c and 2e), which is very similar to the pattern in Figure 1, although the simulated round cell does not split into two as observed. Why does this deformation occur? Second, although the crescent cell includes a substantial viscous cell, the conjugate round cell in the opposite hemisphere does not. Viscous cells are considered to be excited in the equatorial region. In section 3.1, we determine viscous cells in the equatorial plane. Point r (point s) in Figure 2 shows the projection of the equatorial viscous cell center to the round (crescent) cell hemisphere. In the crescent cell hemisphere, the viscous cell appears almost intact, naturally embedded in the merging cell. In contrast, in the round cell hemisphere, the original viscous cell in the equatorial plane is overall obliterated by the merging cell. Where does this interhemispheric difference come from? Actually the round cell deformation and the interhemispheric viscous cell asymmetry are closely related. The goal of this paper is to elucidate the relation between the viscous cell and the round cell and clarify its dipole tilt dependence. For this purpose, in section 3, we first explore the magnetospheric convection, both viscous-driven and reconnection-driven. To understand these processes, one needs to know the geometry and topology of the magnetosphere. We then in section 4 return to Figure 2 and discuss the dipole tilt effect on the ionospheric convection. We consider how the viscous-driven convection and the reconnection-driven convection mutually affect each other in the ionosphere.

3. Structure of the Magnetosphere: Geometrical Relationship Between the Viscous Circulation and the Dungey Circulation

3.1. Viscous Cells

[11] We first describe the geometry of the viscous cells generated in the equatorial region. In the simulated magnetosphere-ionosphere system in this paper, in addition to reconnection-driven convection, "viscous convection" plays an important role. By the word "viscous convection," we mean that, when looking downward on the equatorial plane from the north, there are a clockwise convection cell on the dawnside and a counterclockwise convection cell on the duskside circulating in the closed field line region. Note that this identification is purely morphological even though its name suggests a physical process. The name "viscous" derives from the suggestion by *Axford and Hines* [1961, Figure 3] that the viscous-like interaction between the solar wind and the magnetospheric plasma excites two convection cells in the magnetosphere. In the BATS-R-US code, however, there is no physical viscosity in the governing equations. It is known nevertheless that ideal-MHD simula-

Figure 2. Ionospheric potential contours (solid lines) for (a, b) $D = 0°$, (c, d) $D = -20°$, and (e, f) $D = -35°$ in the northern ionosphere (Figures 2a, 2c, and 2e) and southern ionosphere (Figures 2b, 2d, and 2f). The polar azimuthal equidistant projection is used. The contours are labeled every 6 kV. The large dotted loop centered on the geomagnetic pole shows the open-closed field line boundary (i.e., polar cap boundary). Point m in Figures 2a, 2c, and 2e represents the topological cusp in the Northern Hemisphere (the foot point of stemline s_1 in Figure 4), while point n in Figures 2b, 2d, and 2f represents the topological cusp in the Southern Hemisphere (the foot point of stemline s_2 in Figure 4). Point a (point d) represents the center of the round cell (crescent cell). Point b (point c) shows the location of the potential peak on the polar cap boundary on the round cell side (crescent cell side). Point r (point s) represents the ionospheric projection of the equatorial viscous cell center to the round cell (crescent cell) hemisphere. The small dotted loop passing through point b and centered on point a is the demarcation contour between the lobe cell and the merging cell. The dotted loop passing through point c and centered on point d (only part of it is seen for Figures 2d and 2f) is the demarcation contour between the viscous cell and the merging cell.

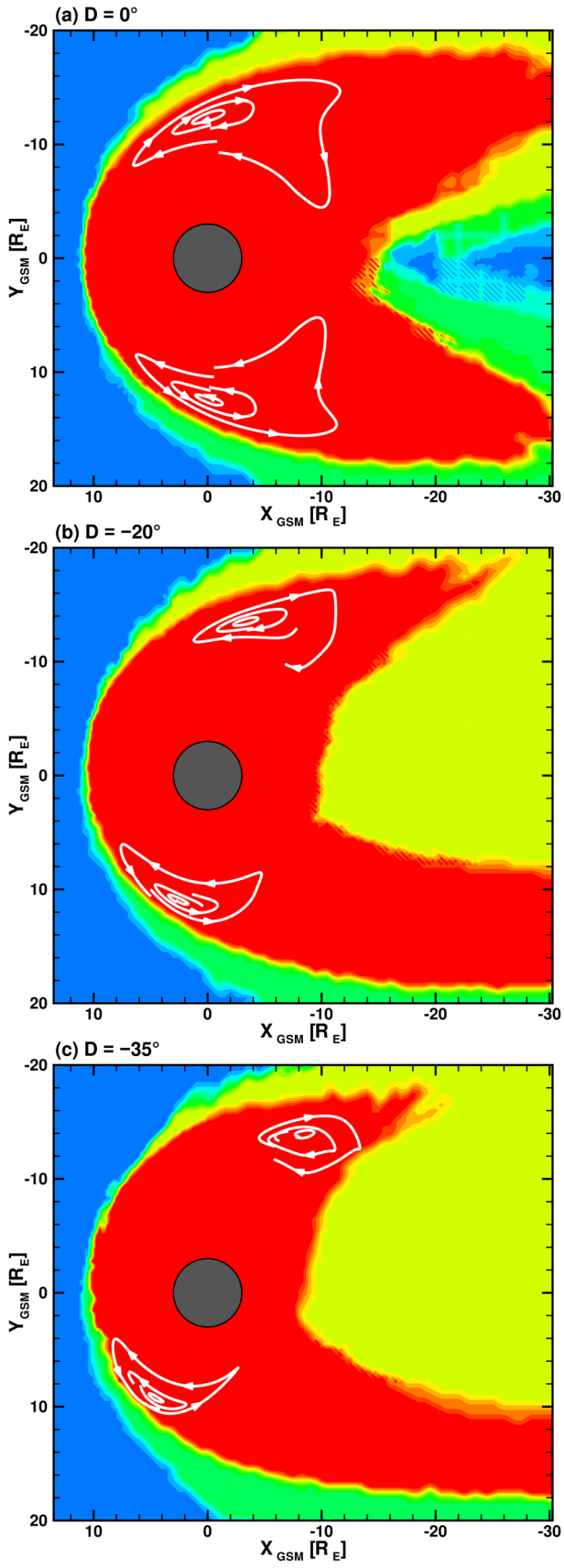

tions can reproduce the "viscous cells" morphologically, with the cells conceivably driven by numerical viscosity. This situation is similar to that of reconnection driven by numerical resistivity in ideal-MHD simulations. However, while we empirically know that reconnection resulting from numerical resistivity in magnetospheric simulations can reproduce the magnetospheric morphology reasonably well, the effects of numerical viscosity in this context have not been studied extensively. Thus the issue of how well our simulation can reproduce the actual viscous cells (if they exist) in the magnetosphere remains an open problem.

[12] Figure 3 shows the three-dimensional streamlines in the equatorial region (white lines with arrows) projected along the GSM Z axis to the GSM equatorial plane, for $D = 0°$ (Figure 3a), $D = -20°$ (Figure 3b), and $D = -35°$ (Figure 3c). Streamlines are determined using only the field-perpendicular component of the plasma velocity (i.e., $\mathbf{v}_\perp \equiv \mathbf{v} - (\mathbf{v} \cdot \mathbf{b})\mathbf{b}$, where $\mathbf{v}$ is the plasma velocity and $\mathbf{b}$ is the unit vector along the magnetic field). The streamlines are helices along the magnetic field. We note here that the streamlines projected along the magnetic field to a reference plane (not shown here) do not close exactly. This is not surprising because the viscosity (which is expected to be centered on the equatorial plane) can produce nonidealness (i.e., $\mathbf{E} + \mathbf{v} \times \mathbf{B} \neq \mathbf{0}$, where $\mathbf{E}$ and $\mathbf{B}$ represent the electric and magnetic fields, respectively). In the background of Figure 3, the topological regions are shown by colors: red (closed field region), blue (IMF region), greenish yellow (NL), and green (SL). In the equatorial plane, a clockwise vortex lies on the dawnside and a counterclockwise vortex on the duskside. These are numerically produced viscous cells.

3.2. Magnetospheric Topology

[13] Figure 3 indicates that as the dipole tilt increases (decreasing D values), the line connecting the dawnside and duskside cell centers (which approximately passes the center of the Earth) rotates clockwise. We suggest that this clockwise rotation is related to the geometry of the dayside separator which determines the nature of reconnection for given IMF and dipole tilt conditions. A separator is an intersection of separatrices which mark the boundaries between topological regions. Thus we next discuss the topology of the magnetosphere.

[14] It is known that the magnetic topology of the magnetosphere revealed in MHD simulations is equivalent to that obtained when superposing a dipole field and a uniform field in a vacuum [*Crooker et al.*, 1998; *White et al.*, 1998; *Siscoe et al.*, 2001a, 2001b; *Watanabe et al.*, 2005, 2007; *Dorelli et al.*, 2007]. The boundary between the open field line region and the closed field line region is topologically equivalent to a torus, while the boundary between the open field line region and the IMF line region is topologically

Figure 3. Plasma flow vortices (white lines with arrows) near the GSM equatorial plane for (a) $D = 0°$, (b) $D = -20°$, and (c) $D = -35°$. Three-dimensional streamlines of the velocity perpendicular to the magnetic field are projected to the equatorial plane along the Z axis. In the background, four topological regions are represented by color: closed field line region (red), IMF line region (blue), north lobe (NL) (greenish yellow), and south lobe (SL) (green). See color version of this figure in the HTML.

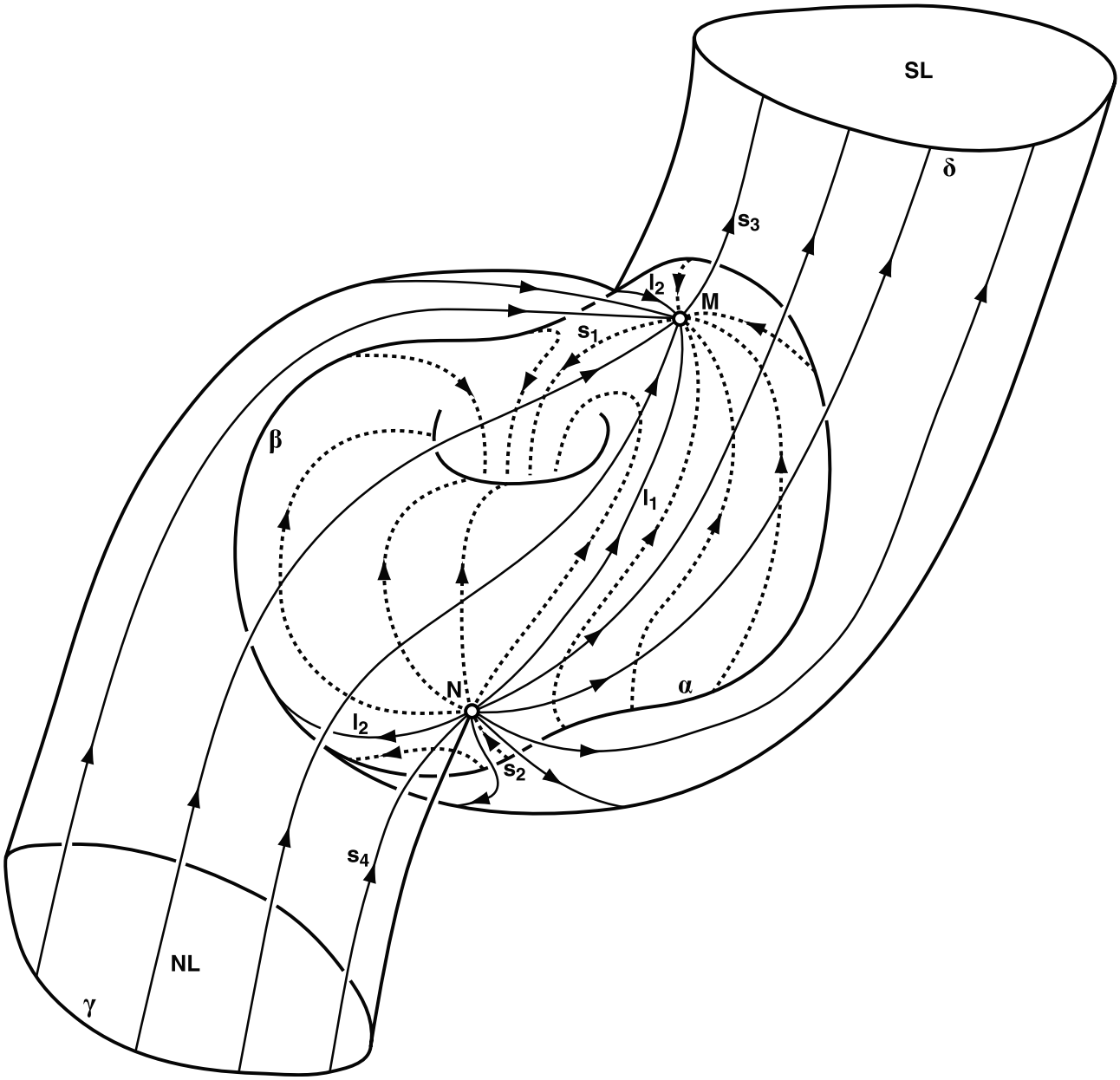

Figure 4. Separatrix surfaces (topologically equivalent to a torus and a cylinder) for northward IMF. Solid lines with arrows represent the field lines on the cylinder surface, while dotted lines with arrows represent the field lines on the torus surface.

equivalent to a cylinder. The torus is touching the cylinder along a circle which consists of two magnetic field lines called separators. There are two magnetic nulls on the separator circle, and the separators connect the two magnetic nulls. Figure 4 shows a simplified schematic of this magnetospheric topology for northward IMF. Here we follow *Watanabe et al.* [2007, Figure 2] and *Watanabe and Sofko* [2008, Figure 1] for the notation signifying magnetic nulls (M and N), separatrices (α, β, γ, and δ), separators (l_1 and l_2), and singular lines (s_1, s_2, s_3, and s_4). Separatrices α and β form a torus, while separatrices γ and δ form a cylinder. Separators l_1 and l_2 lie where the torus and the cylinder meet. Field lines on the torus (cylinder) are shown by dotted (solid) lines with arrows. All the field lines on separatrices α and γ converge to null M, except for the two singular field lines (s_2 on separatrix α and s_4 on separatrix γ) that converge to null N. Similarly, all the field lines on separatrices β and δ diverge from null N, except for the two singular lines (s_1 on separatrix β and s_3 on separatrix δ) that diverge from null M. The singular lines connecting the null points to the ionosphere (s_1 and s_2 in Figure 4) are called "stemlines" [*Siscoe et al.*, 2001b].

[15] The locations of the magnetic null points and separators determine the geometry of the magnetosphere and consequently the types of reconnection that occur for the given IMF orientation and the given dipole tilt. For IMF $B_Y > 0$, the Northern Hemisphere magnetic null (M) is on the duskside, while the Southern Hemisphere magnetic null (N) is on the

Table 1. Null Point Positions in GSM Coordinates

	Northern Hemisphere Null M			Southern Hemisphere Null N		
Dipole Tilt	X (R_E)	Y (R_E)	Z (R_E)	X (R_E)	Y (R_E)	Z (R_E)
$D = 0°$	−1.250	8.250	12.500	−1.250	−8.250	−12.500
$D = -20°$	−8.500	10.000	14.750	2.250	−8.000	−10.500
$D = -35°$	−12.000	9.750	15.250	4.375	−7.750	−9.125

dawnside. If there is no dipole tilt, the dayside separator passes through the subsolar point and roughly lies on the plane $Z = Y\cot\theta_M$ in GSM coordinates, where θ_M is the clock angle of null M ($\theta_M = \mathrm{Arg}(Z_M + iY_M)$). However, when the dipole is tilted, the dayside separator is not in the $Z = Y\cot\theta_M$ plane. Table 1 shows the positions of the null points for the three simulation runs. In the null search, we did not use a sophisticated algorithm such as that proposed by *Greene* [1992]. The null point locations were determined simply by searching a magnetic field minimum on the grid points. This brute-force method is sufficient for the discussion in this paper. For $D = 0°$, the two nulls are symmetric about the X axis, and they are located roughly in the dawn-dusk plane ($X = 0$). The clock angle of null M for $D = 0°$ is $\theta_M = 33°$. In the vacuum superposition model, θ_M is given by $\theta_M = \arctan\left(\frac{\sqrt{8+9\cot^2\theta_c}-3\cot\theta_c}{2}\right)$ ($0° < \theta_c < 180°$) [*Yeh*, 1976]. Our simulation result ($\theta_M = 33°$) shows some deviation from the vacuum superposition model ($\theta_M = 40°$). As the dipole tilt becomes large (with decreasing D), the Northern Hemisphere null (null M) moves away from the Sun, while the Southern Hemisphere null (null N) moves toward the Sun. Accordingly the dayside separator does not pass through the subsolar point.

[16] Figure 5 demonstrates the dayside last closed field lines for $D = -35°$ projected onto the X-Y plane (Figure 5a), Z-X plane (Figure 5b), and Y-Z plane (Figure 5c) in GSM coordinates. Nightside last closed field lines are not shown as they are very hard to visualize clearly and are not essential for our discussion. Blue (red) lines emanate from infinitesimally equatorward of the Southern (Northern) Hemisphere polar cap boundary and converge to the vicinity of null M (null N), forming a surface within separatrix α (separatrix β). This surface virtually represents separatrix α (separatrix β). The field line bundle then goes down to the northern (southern) ionosphere along stemline s_1 (stemline s_2). The dayside juncture of separatrices α and β is separator l_1, a field line which emanates from null N and converges to null M. Although the existence of such a field line is obvious in Figure 5, it is difficult to extract separator l_1 from the simulation data because of numerical errors. In Figure 5, we indicated the expected location of separator l_1 in the equatorial region where blue lines representing separatrix α and red lines representing separatrix β come close together. Figure 5 indicates that the route of the dayside separator l_1 shifts dawnward and northward compared to the route for $D = 0°$ which is approximately in the $Z = Y\cot 33°$ plane. Consequently, in the Y-Z plane in Figure 5c, (blue) separatrix α dominates in the area facing the Sun, which means that SL field lines (which are facing separatrix α) drape over the dayside magnetosphere more than NL field lines (which are facing separatrix β).

3.3. Relation Between the Viscous Cell and the Dungey-Type Merging Cell

[17] As Figure 5a indicates, the dayside separator for $D = -35°$ crosses the GSM equatorial plane at a point about 43° westward of the subsolar point. (The precise location must be determined from Figures 5b and 5c because the equatorial crossing point of l_1 does not correspond to the largest distance from the Z axis.) The equatorial crossing point of separator l_1 is correlated with the positions of the two viscous cells. In order to investigate this relation, we define the azimuth angle ψ of a point (X, Y) on the equatorial plane as $\psi \equiv \mathrm{Arg}\,(X + iY)$. Figure 6 shows the dipole tilt dependence of the azimuth angle of the duskside viscous cell center, the equatorial crossing point of the dayside separator, and the dawnside viscous cell center. Here, the data points for $D \geq 0$ were determined assuming that the configurations for $D = D_0 \geq 0$ are obtained by rotating 180° about the X axis the configurations for $D = -D_0$ (although one must reverse the direction of the magnetic field). This assumption, which we call the rotational symmetry assumption, will be used throughout this paper. Figure 6 indicates that relative to the equatorial crossing point of the dayside separator, the two viscous cells have an angular separation which ranges from 78° to 107° (~90° on average). Figure 7 schematically depicts this geometrical relationship for the $D = -35°$ case (a sketch from Figures 3c and 5a). The equatorial crossing point of the dayside separator (l_1) is located in the prenoon sector. The two viscous cells appear roughly 90° east and west of this point.

[18] There is a simple interpretation of the geometrical relationship between the viscous cell positions and the equatorial crossing point of the dayside separator. The viscous cell always appears inside the Dungey-type merging cell. Thus the location of the viscous cell is constrained by the location of the Dungey-type merging cell. In turn, the Dungey-type merging cell is constrained by the geometry of the separatrices. For the $B_Y > 0$ case we are considering, the duskside Dungey cycle is driven by two kinds of Dungey-type reconnection:

$$\text{Closed-}\alpha + \text{IMF-}\gamma \rightarrow \text{NL} + \text{SL}\ \ (\text{type A+}), \tag{1}$$

$$\text{NL} + \text{SL} \rightarrow \text{Closed-}\alpha + \text{IMF-}\gamma\ \ (\text{type G+}), \tag{2}$$

where Closed-α represents field lines in the closed field line region adjacent to separatrix α, whereas IMF-γ represents field lines in the IMF line region adjacent to separatrix γ. We also use Closed-α and IMF-γ to represent the topological regions occupied by those field lines [see *Watanabe et al.*, 2005, 2007]. The open-closed flux transport associated with the duskside Dungey cycle occurs through separatrix α. Therefore the duskside Dungey-type merging cell is formed in the regions adjacent to separatrix α. The duskside dotted loop in Figure 7 (M_D) represents the duskside Dungey-type merging cell in the equatorial plane. Note that M_D represents the conceptual Dungey-type merging cell projected to the equatorial plane along the field lines. Actually there is no such two-dimensional closed orbit in the equatorial plane. Also the three-dimensional orbit does not close, as we noted in the viscous cells in Figure 3. The three-dimensional Dungey cycle on the duskside is represented by a quasipe-

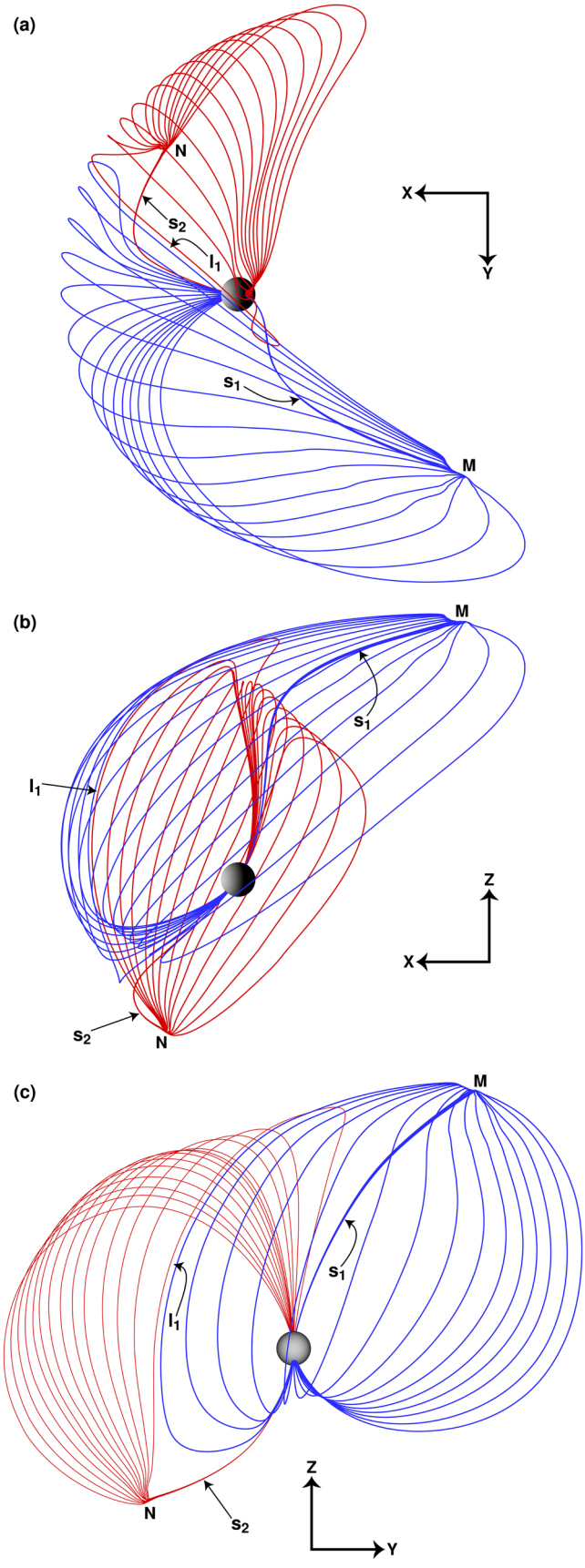

riodic helical orbit that occupies the southern dusk quadrant. Point A_3 (point G_1) in Figure 7 is the point where the streamline crosses separatrix α by type A+ reconnection (type G+ reconnection) (we follow the notation of *Watanabe and Sofko* [2008, Figures 2 and 4]). The position of the duskside viscous cell is determined by the position of point A_3, and in turn, the position of point A_3 is determined by the position of separator l_1.

[19] In the traditional view, the viscous cell is excited owing to the flow shear between the magnetosheath and the adjacent closed low-latitude boundary layer [*Axford and Hines*, 1961]. This traditional view must be modified. In the simulated magnetosphere, the viscous cell is excited owing to the flow shear between the lobe and the adjacent closed field line region. For the duskside circulation in Figure 7, the viscous cell is driven because the antisunward flow in the postnoon SL (which is part of the Dungey-type merging cell) drags the plasma in the adjacent Closed-α region. The antisunward flow excited in the closed field line region returns to the dayside to form a viscous cell, although its mechanism is not necessarily clear. The sunward return flow of the Dungey-type merging cell must be located Earthward of the viscous cell in order to maintain steady state convection (for otherwise the viscous cell and the Dungey-type merging cell would be mixed). The above argument indicates that the viscous cell and the Dungey-type merging cell are not totally independent. Rather, it may be said that the viscous cell is formed as a consequence of the Dungey-type merging cell.

[20] The same holds true for the dawnside circulation. The dawnside Dungey cycle is driven by another two kinds of Dungey-type reconnection:

$$\text{Closed-}\beta + \text{IMF-}\delta \rightarrow \text{NL} + \text{SL (type B}-), \tag{3}$$

$$\text{NL} + \text{SL} \rightarrow \text{Closed-}\beta + \text{IMF-}\delta \text{ (type H}-), \tag{4}$$

where Closed-β represents field lines in the closed field line region adjacent to separatrix β, whereas IMF-δ represents field lines in the IMF line region adjacent to separatrix δ [see *Watanabe et al.*, 2005, 2007]. Therefore the dawnside Dungey-type merging cell is formed in the regions adjacent to separatrix β. The dawnside dotted loop in Figure 7 (M_D) conceptually represents the dawnside Dungey-type merging cell in the equatorial plane. Three-dimensionally, the Dungey cycle on the dawnside is represented by a quasiperiodic helical orbit that occupies the northern dawn quadrant. Point B_1 (point H_3) in Figure 7 is the point where the streamline crosses separatrix β by type B− reconnection (type H− reconnection) (we follow the notation of *Watanabe*

Figure 5. Dayside last closed field lines for $D = -35°$ projected onto the (a) *X*-*Y* plane, (b) *Z*-*X* plane, and (c) *Y*-*Z* plane in GSM coordinates. Blue (red) lines emanate from the southern (northern) polar cap boundary, converge to null M (null N) in the Northern (Southern) Hemisphere, and go down to the northern (southern) ionosphere along stemline s_1 (stemline s_2). There should be a field line l_1 demarcating the separatrix represented by blue lines and the separatrix represented by red lines. This line is the dayside separator connecting null M and null N. See color version of this figure in the HTML.

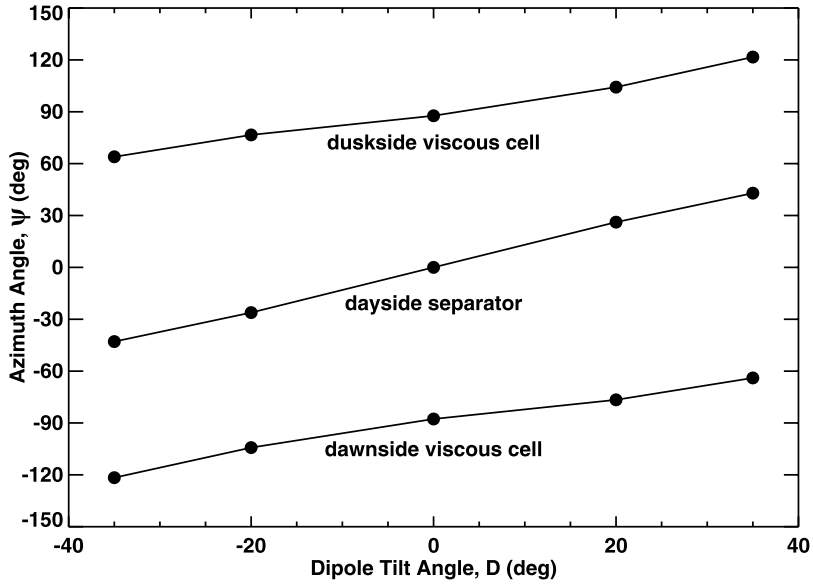

Figure 6. The dipole tilt dependence of the azimuth angles of the vortex centers in the equatorial plane and the equatorial crossing point of the dayside separator, for IMF $\theta_c = 63°$. The data points for $D \geq 0$ were determined from the simulation results for $D \leq 0$ by assuming the rotational symmetry (see text).

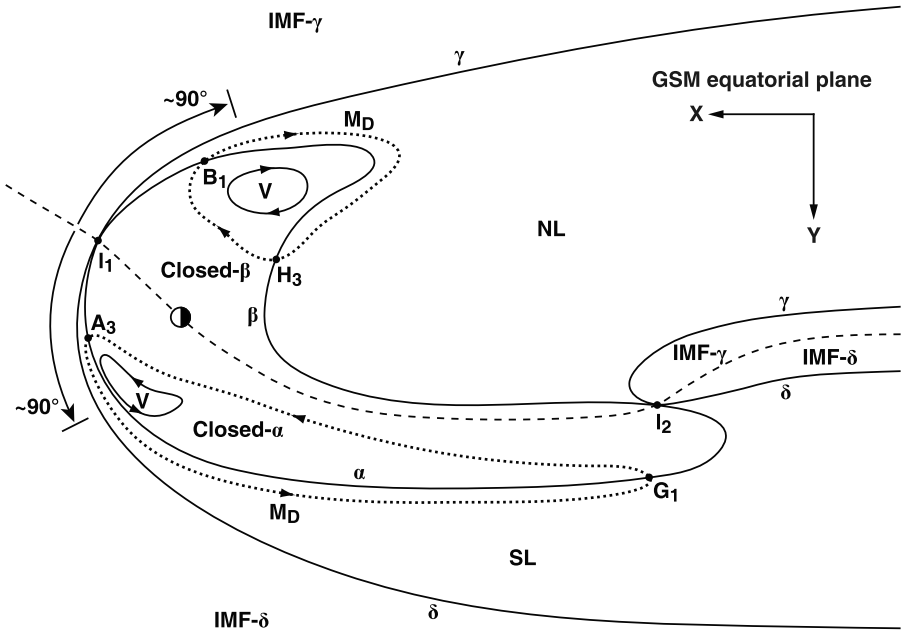

Figure 7. A sketch for the $D = -35°$ case showing the geometrical relationship between the dayside separator (l_1) and the equatorial viscous cells (V). Separatrices (α, β, γ, and δ) divide the entire space into six topological regions (IMF-γ, IMF-δ, NL, SL, Closed-α, and Closed-β). The dashed line represents the demarcation between IMF-γ and IMF-δ and between Closed-α and Closed-β. The dotted loops (M_D) represent the dawnside and duskside Dungey cycles projected to the equatorial plane along the field lines. Note that there are no such two-dimensional closed orbits in the equatorial plane. Three-dimensional Dungey cycles are found in the northern dawn quadrant and in the southern dusk quadrant as quasi-periodic helical orbits. Points B_1, H_3, A_3, and G_1 represent the points where the Dungey cycle orbit crosses the separatrix.

and Sofko [2008, Figures 3 and 5]). The position of the dawnside viscous cell is determined by the position of point B_1, and in turn, the position of point B_1 is determined by the position of separator l_1.

[21] The dashed line in Figure 7 conceptually represents the demarcation between Closed-α and Closed-β and between IMF-γ and IMF-δ. For the convection system during IMF B_Y-dominated periods, the dashed line also represents the demarcation between the dawnside circulation and the duskside circulation. In the steady state convection system, there is no magnetic flux transport across the dashed line. Here the "steady state" means that the magnetic topology in Figure 4 is conserved at any point of time. Plasma flow across the dashed line indicates the mixture of dawnside and duskside circulations, which is only possible when the null-separator structure in Figure 4 breaks down, at least temporally. As the magnitude of the dipole tilt increases, the demarcation line in the closed field line region rotates clockwise for $D < 0$ or counterclockwise for $D > 0$. The azimuth angles of Dungey-type merging cells and the embedded viscous cell also rotate clockwise or counterclockwise accordingly.

4. Dipole Tilt Effects on the Ionospheric Convection Pattern

4.1. Ideal Convection Pattern

[22] To begin with, we discuss the expected ionospheric convection (or potential) pattern for the ideal case; that is, $\mathbf{E} + \mathbf{v} \times \mathbf{B} = \mathbf{0}$ everywhere except in the portions of the equatorial region where the viscous cells are generated and the diffusion regions on the separatrices where reconnection takes place. The diffusion region is characterized by a nonvanishing parallel (field-aligned) electric field. However, since the simulation code solves the equations of ideal MHD, it is in principle impossible to identify the diffusion regions in the simulated magnetosphere. Yet we infer that, except for the nightside Dungey-type reconnection, the diffusion regions are located at high latitudes near the magnetic null points where antiparallel field line geometry tends to occur. In addition, because the diffusion region has a three-dimensional extent, the ionospheric projection of the diffusion region is a two-dimensional area. Since we do not know the exact extent of the diffusion region or the spatial distribution of the parallel electric field, it is very difficult to examine the ionospheric potentials in this problem setting. However, we can gain insight into this problem by employing the "current penetration model" of *Watanabe et al.* [2007], which provides basically the same ionospheric consequences as the original three-dimensional diffusion region case. The name "current penetration model" was introduced by *Siscoe* [1988] to describe the merging models that allow a normal component of the magnetic field on the separatrix. This class of merging models was first proposed by *Alekseyev and Belen'kaya* [1983]. In the current penetration model of *Watanabe et al.* [2007], the diffusion region is represented by a field line segment on the separatrix (which we call the X line), with a small magnetic field component normal to the separatrix in the vicinity of the X line. This configuration is considered to be the limit when the three-dimensional diffusion region collapses into a line on the MHD scale. The merit of this model is that the electric field along the X line is directly mapped to the ionosphere as a perpendicular (to **B**) electric field.

[23] Figure 8 shows the duskside convection pattern in the Northern Hemisphere (Figures 8a and 8b) and the Southern Hemisphere (Figure 8c) for IMF $B_Y > 0$. The difference between Figures 8a and 8b is that while Figure 8a shows a simple superposition of convection cell elements, Figure 8b shows the resultant net convection. The patterns in Figures 8a and 8c are basically the same as those described by *Watanabe et al.* [2007, Figure 9] and *Watanabe and Sofko* [2008, Figure 6], except for the addition of a viscous cell. In the discussion in section 3.3 of the reconnection-driven equatorial convection on the duskside, we only needed to consider Dungey-type reconnection (type A+ and type G+). In the ionosphere, however, we also need to consider two kinds of interchange-type reconnection contributing to the duskside convection system:

$$\text{IMF-}\gamma + \text{NL} \rightarrow \text{NL} + \text{IMF-}\gamma \ (\text{type C}-), \tag{5}$$

$$\text{SL} + \text{Closed-}\alpha \rightarrow \text{Closed-}\alpha + \text{SL} \ (\text{type E}+). \tag{6}$$

The thick solid lines in Figure 8 are projected X lines with symbols A_3, A_4, C_4, E_1, E_3, E_4, G_1, and G_4 corresponding to those of *Watanabe et al.* [2007, Figure 7] and *Watanabe and Sofko* [2008, Figures 2 and 4]. The kernel letters (A, C, E, and G) represent the location of the diffusion region. The duskside portion of G_4 in Figures 8a and 8b is drawn with a dotted line in order to show that type G+ reconnection is not active on the duskside flank. Lines A_3 and G_1 in Figure 8c correspond to points A_3 and G_1 in Figure 7, respectively. That is, the convection cell labeled M_D in Figure 8c is the ionospheric projection of the duskside Dungey-type merging cell in Figure 7. The dashed loop (partly overlapped with the projected X lines) is the polar cap boundary, which is the ionospheric cross section of separatrix β (Figures 8a and 8b) or separatrix α (Figure 8c). Point m in Figures 8a and 8b (point n in Figure 8c) is the foot point of stemline s_1 (stemline s_2) coming from null M (null N). The streamlines in Figures 8a and 8c show the four elemental convection cells: lobe cell (L), Dungey-type merging cell (M_D), hybrid merging cell (M_H), and viscous cell (V). For the discussion below, we assume that each streamline corresponds to a potential drop of Φ (the streamlines are equivalent to equipotential contours drawn every Φ). That is, the potential drop of each convection cell is represented as $\Phi_L = \Phi$ (lobe cell), $\Phi_{MD} = \Phi$ (Dungey-type merging cell), $\Phi_{MH} = \Phi$ (hybrid merging cell), and $\Phi_V = \Phi$ (viscous cell).

[24] Let us first examine the Southern Hemisphere convection. In Figure 8c, we consider the case in which the X lines E_1 and A_3 overlap, as do the X lines E_3 and G_1 [*Watanabe and Sofko*, 2008, Figure 7a]. The resultant convection is the normal (nonsplit) crescent cell which is the most commonly observed pattern in the crescent cell hemisphere. The X line overlapping means that the magnetic flux transports across separatrix α both by Dungey-type reconnection (type A+ and type G+) and by lobe-closed interchange reconnection (type E+) are canceled. Since the

diffusion regions on the duskside are located in the Northern Hemisphere, the effect of type E+ reconnection that emerges south of the diffusion regions is only a reduction of the Dungey-type merging cell potential. This is the reason why in section 3.3 we did not need to consider the effect of type E+ reconnection in the equatorial plane. Thus only the Dungey-type merging cell appears in the equatorial plane, with the viscous cell embedded in it. This convection pattern is mapped directly to the ionosphere in the Southern Hemisphere. Consequently, the viscous cell in the southern ionosphere remains almost intact. The shaded region in Figure 8c represents the projection of the equatorial viscous cell. The viscous cell meets the polar cap along a finite length segment of the polar cap boundary.

[25] The situation in the Northern Hemisphere is completely different. Figure 8a represents a simple superposition of the reconnection-driven streamlines and the viscous-driven streamlines. The coupling of lobe-closed interchange reconnection (type E+) and Dungey-type reconnection (type A+ and type G+) produces a hybrid merging cell circulating outside the lobe cell and inside the Dungey-type merging cell. The shaded area shows the projection of the equatorial viscous cell. It touches the polar cap boundary only at the topological cusp (point m). In the ideal case, the effect of the viscous cell is confined to this shaded area. Since the shaded area connects to the topological cusp, the viscous cell streamline and the hybrid merging cell streamline in the superposed convection pattern inevitably intersect, which means that the two convection cells partly share common field lines. Since both the antisunward flow of the viscous cell and the sunward flow of the hybrid merging cell are excited in the closed field line region adjacent to the separatrix, the opposing flows are for the most part on the same field lines and cancel each other in the ionosphere. In the ideal case, the resultant convection pattern is expressed by the linear superposition of the viscous cell potential and the hybrid merging cell potential. The actual form of the superposed potential depends on how the two cells overlap. However, considering all the possible cases of the overlapping is not only complicated but also unpractical, because they include some unrealistic overlapping situations. Therefore we here consider only one simple but sufficiently realistic case illustrated in Figure 9. For this case, the center of the viscous cell (point r) is located on the outer edge of the hybrid merging cell so that the antisunward flow region of the viscous cell exactly corresponds to the sunward flow region of the hybrid merging cell. This assumption is sufficient for the qualitative discussion in this paper. In Figure 9, point b is the potential peak on the polar cap boundary. In the ideal case, point b should be the topological cusp where the viscous cell and the lobe cell meet on the separatrix.

[26] Figure 8b shows the resultant convection pattern in the Northern Hemisphere. The viscous cell with a potential

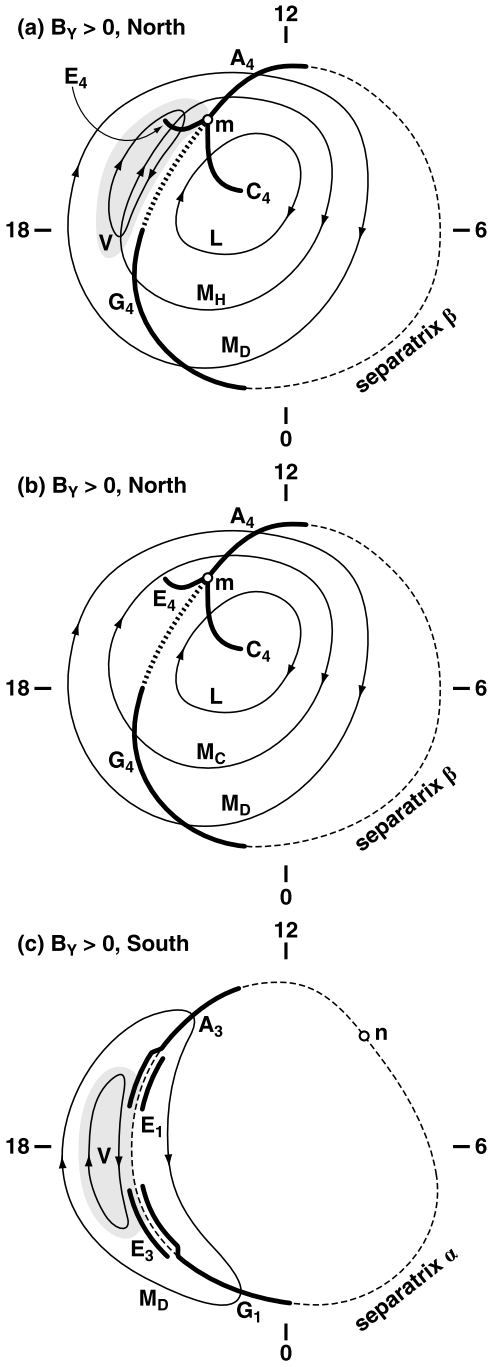

Figure 8. Duskside "ideal" ionospheric convection for IMF $B_Y > 0$ in the (a, b) Northern Hemisphere and (c) Southern Hemisphere. Thick solid lines represent the ionospheric projection of the X lines (A_3, A_4, C_4, E_1, E_3, E_4, G_1, and G_4). The dashed loop (partly overlapped with the projected X lines) represents the open-closed field line boundary. The duskside portion of G_4 in Figures 8a and 8b is drawn with a dotted line in order to show that type G+ reconnection is not active on the duskside flank. Point m (point n) is the topological cusp in the northern (southern) ionosphere, which is the foot point of stemline s_1 (stemline s_2). While Figure 8a represents the simple superposition of convection cell elements, Figure 8b shows the resultant convection pattern. In Figures 8a and 8c, the shaded area shows the projection of the equatorial viscous cell. Convection cells are denoted by M_D (Dungey-type merging cell), M_H (hybrid merging cell), V (viscous cell), and M_C (coalescent merging cell). Each streamline is assumed to represent a potential drop of Φ.

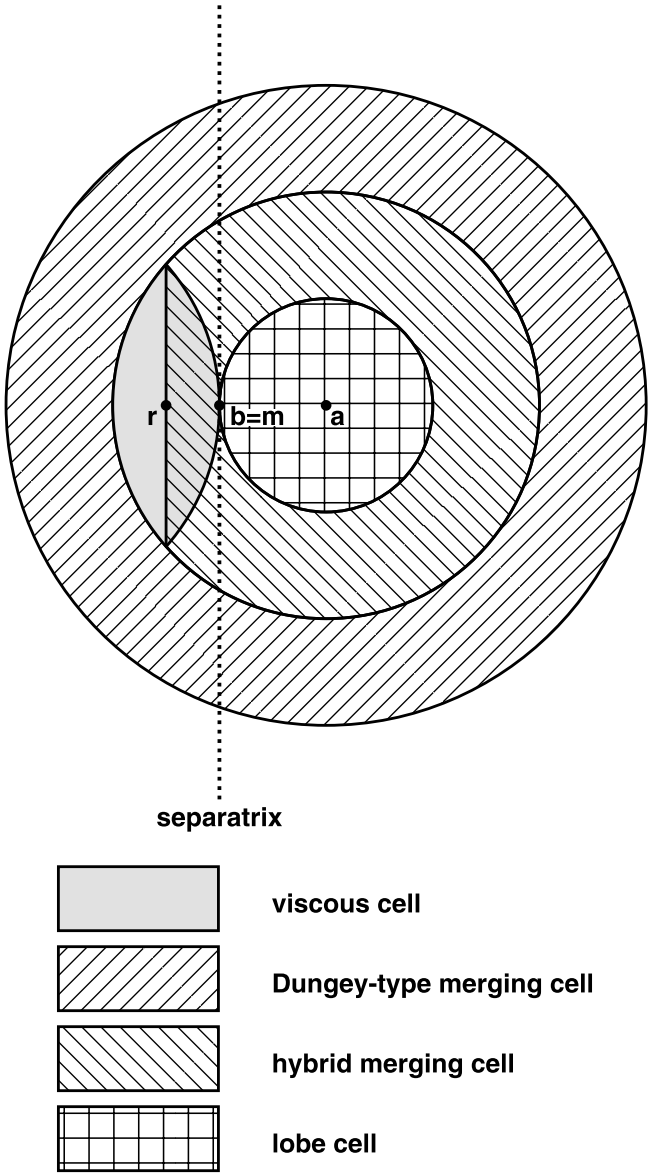

Figure 9. The spatial relationship of the four elemental convection cells in the duskside northern ionosphere for $B_Y > 0$, with noon to the top and dusk to the left. Point a, point b, and point r represent the center of the lobe cell, the potential peak on the polar cap boundary (which should be the topological cusp in the ideal case), and the center of the viscous cell, respectively. In this paper, we discuss only the case when point r is located on the equatorward edge of the hybrid merging cell.

drop of Φ and the hybrid merging cell with a potential drop of Φ are incorporated into one large merging cell (which we call the "coalescent merging cell," denoted as M_C) with a potential drop of Φ. This incorporation is the result of simple linear superposition of the viscous cell potential and the hybrid merging cell potential, and no additional field-aligned potential drop is required. This feature contrasts with the incorporation of two nonintersecting convection cells. For the latter case, the coalescence of two convection cells each having a potential drop of Φ to form one convection cell with a potential drop of Φ requires a field-aligned potential drop of Φ [*Watanabe and Sofko*, 2009c, section 4]. The potential drop of the resultant coalescent merging cell (Φ_{MC}) is the same as the potential drop of the original hybrid merging cell (i.e., $\Phi_{MC} = \Phi_{MH}$). In Figure 8, we considered the incorporation in the $\Phi_V = \Phi_{MH}$ case with the assumption in Figure 9. The results can be extended to the $\Phi_V \neq \Phi_{MH}$ case with the same assumption. The relation $\Phi_{MC} = \Phi_{MH}$ also holds true for $\Phi_V \neq \Phi_{MH}$. For the $\Phi_V \leq \Phi_{MH}$ case, the incorporation produces only a coalescent merging cell, while for the $\Phi_V > \Phi_{MH}$ case, the incorporation produces a coalescent merging cell and a "remnant" viscous cell.

[27] It is clear from the above discussion that the round cell deformation results from the coalescence of the hybrid merging cell and the viscous cell. It is suggested therefore that the resultant round cell geometry is determined directly by the relative position and the relative intensity (potential drop) of the hybrid merging cell and the viscous cell. The positions and intensities of other convection cells would also affect the round cell geometry indirectly. Thus, in the following three sections, we examine the intensities (section 4.2) and positions (section 4.3) of the relevant convection cells revealed in the simulation and consider the combined effects of the viscous cell and the hybrid merging cell that produce the deformation of the round cell (section 4.4).

4.2. Intensity of Each Constituent Cell

[28] We now return to Figure 2 and compare the simulation results with the ideal convection pattern in Figure 8. In this section we examine the intensity of each elemental convection cell. Before entering into a detailed discussion, we draw attention to the following aspect of our analysis. In this paper, we discuss the dipole tilt effects on the duskside convection system for IMF $B_Y > 0$. In this case, the round (crescent) cell appears in the Northern (Southern) Hemisphere. From the rotational symmetry assumption, the dawnside convection pattern in Figure 2 represents the duskside convection pattern for $D \geq 0$ in the opposite hemisphere. For example, the dawnside crescent cell in Figure 2e is equivalent to the duskside crescent cell in the Southern Hemisphere for $D = +35°$, while the dawnside round cell in Figure 2f is equivalent to the duskside round cell in the Northern Hemisphere for $D = +35°$. The rotational symmetry assumption permits easy synthesis of the duskside and dawnside convection patterns from Figure 2.

[29] Figure 2 indicates that, for all the six cases, the potential contours exhibit the basic round/crescent cell pattern as expected in Figures 8b and 8c. One significant difference, though, is the location of the potential peak on the round-cell-side polar cap boundary (point b in Figure 2). In light of Figure 8b, point b should be located at the topological cusp (point m or point n). However, in all six cases, point b shifts antisunward from the topological cusp. The potential difference between point b and the topological cusp ranges from 0.2 kV (Figure 2e) to 3.0 kV (Figure 2a). At the end of this section, we will provide one explanation of this antisunward shift of the potential peak.

[30] We denote the potential values at points a–d in Figure 2 by φ_a, φ_b, φ_c, and φ_d, respectively. In view of Figures 8b

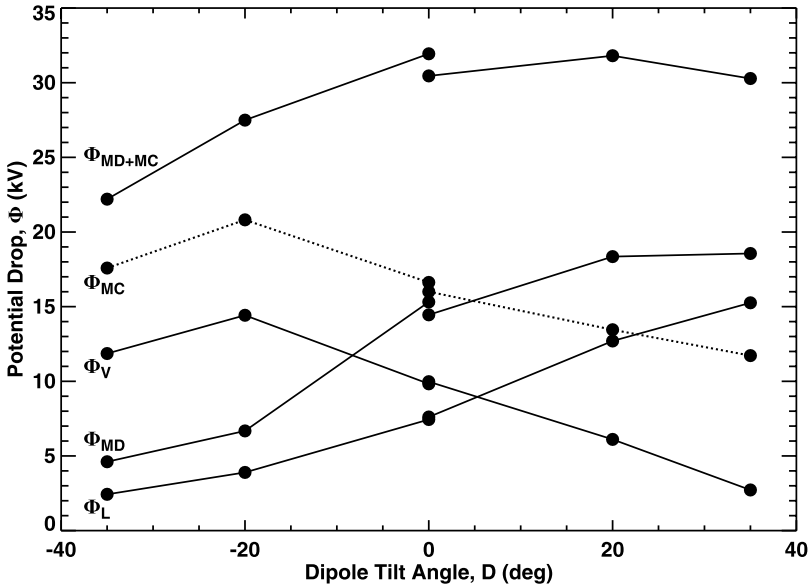

Figure 10. The dipole tilt dependence of the total merging cell potential (Φ_{MD+MC}), coalescent merging cell potential (Φ_{MC}), viscous cell potential (Φ_V), Dungey-type merging cell potential (Φ_{MD}), and lobe cell potential (Φ_L), on the duskside for IMF $\theta_c = 63°$. The Φ_{MC} line is dotted for clarity. The data points for $D \geq 0$ were determined from the simulation results for $D \leq 0$ by assuming the rotational symmetry.

and 8c, the potential drop of each convection cell is given by the following:

$$\Phi_L = |\varphi_a| - |\varphi_b|, \tag{7}$$

$$\Phi_V = |\varphi_d| - |\varphi_c|, \tag{8}$$

$$\Phi_{MD+MC} = |\varphi_b|, \tag{9}$$

$$\Phi_{MD} = |\varphi_c|, \tag{10}$$

$$\Phi_{MC} = |\varphi_b| - |\varphi_c|, \tag{11}$$

where the notation Φ_{MD+MC} is newly introduced here. Let us review these potentials all together. The voltage Φ_L (Φ_V) represents the lobe (viscous) cell potential. Since the potential is zero at the equatorward edge of the merging cell, Φ_{MD+MC} (Φ_{MD}) represents the potential of the merging-cell-proper part of the round (crescent) cell. That is, Φ_{MD+MC} is the sum of the Dungey-type merging cell potential and the coalescent merging cell potential, while Φ_{MD} is the potential of the Dungey-type merging cell. Consequently, Φ_{MC} represents the potential of the coalescent merging cell.

[31] Figure 10 shows the dipole tilt dependence of Φ_{MD+MC}, Φ_{MC}, Φ_V, Φ_{MD}, and Φ_L on the duskside for IMF $B_Y > 0$. The data points for $D \geq 0$ were determined from the simulation results on the dawnside, using the rotational symmetry assumption. The line for Φ_{MC} is shown dotted for clarity. The total merging cell potential (Φ_{MD+MC}), Dungey-type merging cell potential (Φ_{MD}), and lobe cell potential (Φ_L) increase with increasing dipole tilt angle (D), although a saturation is seen in Φ_{MD+MC}. This D dependence is reasonable geometrically because both IMF-closed reconnection and IMF-lobe reconnection are expected to be enhanced in the summer hemisphere and diminished in the winter hemisphere (here $D > 0$ means Northern Hemisphere summer). In contrast, Φ_{MC} and Φ_V decrease with increasing D for $D > -20°$. In addition, Φ_{MC} and Φ_V exhibit very similar trends.

[32] We first consider the viscous cell. Since the viscous cell is directly mapped to the crescent cell hemisphere, it is expected that the trend in Φ_V essentially represents the trend in the equatorial viscous cell potential. In section 3.1, we saw that the viscous cell position in the equatorial plane depends on the dipole tilt. It is thus suggested that the intensity of the viscous cell depends on the position where it is formed, such that the viscous cell intensity becomes larger (smaller) when the cell is formed sunward (tailward) of the dawn-dusk line. The physical mechanism for this intensity variation is not known.

[33] We next consider the coalescent merging cell. As noted in section 4.1, in the ideal case, Φ_{MC} is equal to Φ_{MH} which represents the reconnection potential arising from lobe-closed interchange reconnection. As D increases, the amount of overdraped SL flux decreases (discussion in section 3.2). Consequently the potential of lobe-closed reconnection is also expected to decrease, which would partly explain the decreasing trend of Φ_{MC}. However, in relation to the high correlation between Φ_{MC} and Φ_V, one must check the independence of the two variables. When the hybrid merging cell and the viscous cell coalesce, as we show below, the configuration of the resultant coalescent cell is not stable. Therefore some diffusive processes can change the potential pattern around the separatrix. In this nonideal case, $\Phi_{MC} \neq \Phi_{MH}$ and Φ_{MC} does not represent the reconnection voltage of lobe-closed reconnection.

[34] That Φ_{MC} does not necessarily represent the reconnection potential of lobe-closed reconnection is qualitatively

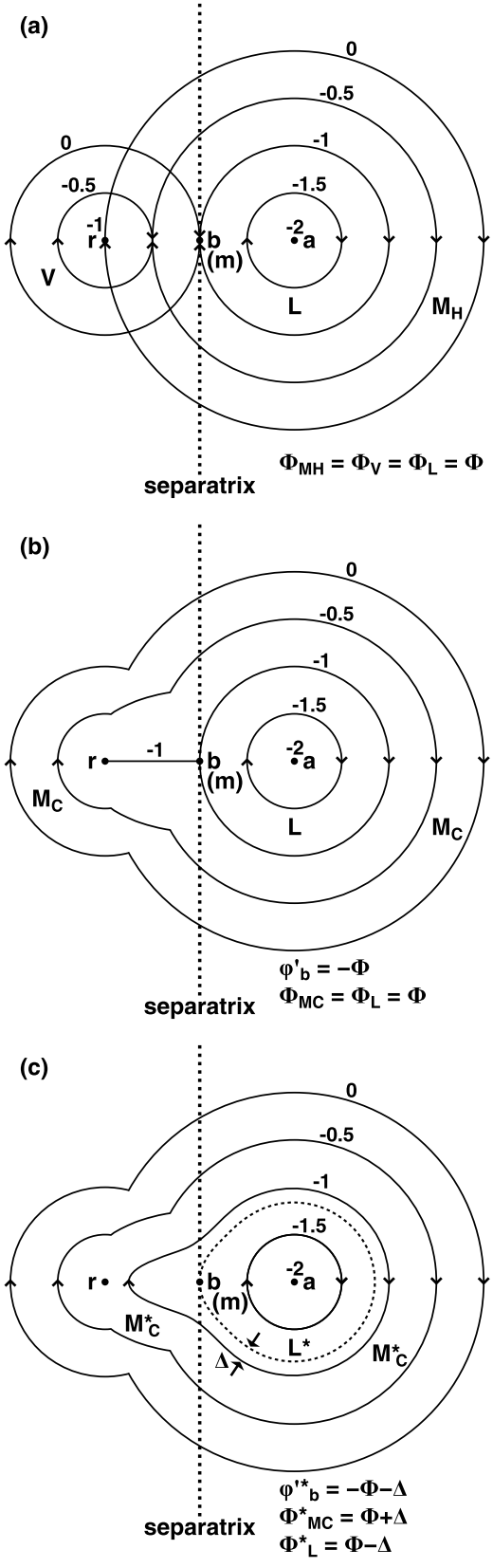

understood as follows. As before, we assume $\Phi_{MH} = \Phi_V = \Phi_L = \Phi_{MD} = \Phi$. For simplicity, we consider a superposition of a circular viscous cell and a circular hybrid merging cell as shown in Figure 11a. Here the Dungey-type merging cell encompassing the viscous cell and the hybrid merging cell (see Figure 9) is not shown because it is irrelevant to the potential superposition. In calculating the superposed potentials, it is convenient to set the zero potential (the reference potential) at the inner edge of the Dungey-type merging cell (where the potential is $\varphi = \varphi_0 = -\Phi$). Thus, in Figure 11, we tentatively work with a shifted potential (φ') defined as $\varphi' = \varphi - \varphi_0 = \varphi + \Phi$. The potential at the viscous (lobe) cell center is lower by Φ (2Φ) than the inner edge of the Dungey-type merging cell. Figure 11b shows the superposed potential pattern. In the absence of diffusion, the potential at point b is $\varphi'_b = -\Phi$, with the lobe cell intact. The potential of the coalescent merging cell is $\Phi_{MC} = \Phi$. However, the segment b-r becomes a null line of the velocity field, and the potential pattern is unstable. Thus it is expected that the potentials near point b could easily transform into the pattern in Figure 11c by a diffusive process. The potential at point b in the presence of diffusion (φ'^*_b) becomes lower by Δ compared to the case in the absence of diffusion: $\varphi'^*_b = \varphi'_b - \Delta$. Therefore the coalescent merging cell potential in the presence of diffusion (Φ^*_{MC}) is higher than the original value by Δ (i.e., $\Phi^*_{MC} = \Phi + \Delta$). At the same time, the lobe cell potential in the presence of diffusion (Φ^*_L) is lower than the original value by Δ (i.e., $\Phi^*_L = \Phi - \Delta$).

[35] As we saw in Figure 11, in the presence of diffusion, the viscous cell acts to increase the potential magnitude on the polar cap boundary. We write this relation as

$$|\varphi^*_b| = |\varphi_b| + \Delta, \tag{12}$$

where φ^*_b (φ_b) represents the potential at point b in the presence (absence) of diffusion and Δ is positive and a function of Φ_V. This potential difference Δ must be provided by a field-aligned potential drop somewhere in the magnetosphere. This drop is also a feature of reconnection

Figure 11. (a–c) Schematics showing how diffusion affects the potential peak on the round-cell-side polar cap boundary. Solid lines represent equipotential contours, with the labeling numbers showing the potentials (measured in Φ) with respect to the inner edge of the Dungey-type merging cell. They equivalently represent streamlines whose flow directions are indicated by arrows. As in Figure 9, point a, point b, and point r represent the center of the lobe cell, the potential peak on the polar cap boundary, and the center of the viscous cell, respectively. Figure 11a shows the simple superposition of the convection cell elements (i.e., a lobe cell L with a potential drop of Φ, a hybrid merging cell M_H with a potential drop of Φ, and a viscous cell V with a potential drop of Φ), while Figure 11b shows the resultant potentials when there is no diffusion (a coalescent merging cell M_C with a potential drop of Φ). In the presence of diffusion, the potentials form a pattern in Figure 11c. Here M^*_C (L^*) represents the coalescent merging (lobe) cell in the presence of diffusion, and Δ is the potential decrement at point b due to the diffusion.

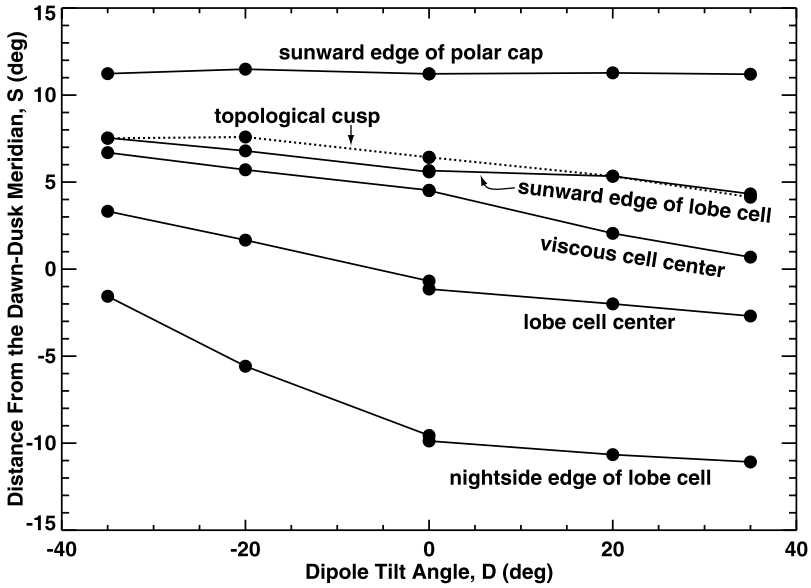

Figure 12. The dipole tilt dependence of the S values (see text) of the sunward edge of the polar cap boundary, the Northern Hemisphere topological cusp (point m), the sunward edge of the lobe cell, the viscous cell center, the lobe cell center, and the tailward edge of the lobe cell, in the duskside northern ionosphere for IMF $\theta_c = 63°$. The line for the topological cusp is dotted for clarity. The data points for $D \geq 0$ were determined from the simulation results for $D \leq 0$ by assuming the rotational symmetry.

in a broad sense [*Schindler et al.*, 1988] but conceptually distinct from the "normal" reconnection which is identified by plasma flow across separatrices. The coalescent merging cell potential in the presence of diffusion (Φ^*_{MC}) is given by

$$\Phi^*_{MC} = |\varphi^*_b| - |\varphi_e| = \Phi_{MC} + \Delta = \Phi_{MH} + \Delta. \quad (13)$$

Here Φ_{MH} is the original hybrid merging cell potential and represents the reconnection voltage of lobe-closed reconnection. Therefore, Φ^*_{MC} overestimates the reconnection voltage of lobe-closed reconnection by Δ. The above discussion also indicates that Φ^*_L underestimates the reconnection voltage of IMF-lobe reconnection by Δ.

[36] At the beginning of this section, we pointed out that the potential peak on the round-cell-side polar cap boundary shifts antisunward from the topological cusp. One probable explanation of this displacement is the viscous cell effect in the presence of diffusion. As we have discussed, the viscous cell acts to increase the magnitude of the potential on the polar cap boundary. If the viscous cell is located antisunward of the topological cusp, the potential peak on the polar cap boundary tends to shift antisunward. This is in agreement with Figure 2, which shows the projected viscous cell center (point r) to be located antisunward of the topological cusp for all cases. *Watanabe et al.* [2007, section 6.1] suggested an alternative explanation of the potential peak shift within the framework of reconnection-driven convection; however, the viscous cell effect described above is a more reasonable interpretation.

4.3. Relative Position of the Viscous Cell and the Lobe Cell

[37] In this section, we examine the relative position of the viscous cell and the hybrid merging cell. One problem here is that we cannot observe the original hybrid merging cell in the simulation. As an obvious alternative, we examine the position of the lobe cell relative to the viscous cell. The hybrid merging cell encompasses the lobe cell, and the extent of the lobe cell (the inner dotted line passing point b in Figure 2) is a good measure of the shape of the hybrid merging cell.

[38] The potential contours in Figure 2 are drawn using a polar azimuthal equidistant projection. In order to discuss the convection pattern quantitatively, we introduce Cartesian coordinates (S, U) to Figure 2. We take the S axis along the SM X axis (midnight to noon) and the U axis along the SM Y axis (dawn to dusk). The origin of the coordinate system is the geomagnetic pole. Thus the position of an ionospheric point is expressed (in degrees) by

$$S = (90 - |\lambda|)\ \cos 15(\chi - 12), \quad (14)$$

$$U = (90 - |\lambda|)\ \sin 15(\chi - 12), \quad (15)$$

where λ and χ are the magnetic latitude of the point in degrees and the magnetic local time of the point in hours, respectively. The value of S represents the signed distance from the dawn-dusk meridian. Dipole tilt effects appear as the sunward or antisunward motion of the points that characterize the convection pattern.

[39] Figure 12 shows, for the duskside northern ionosphere and for IMF $\theta_c = 63°$, the dipole tilt dependence of the S values of the sunward edge of the polar cap, the topological cusp, the sunward edge of the lobe cell, the ionospheric projection of the equatorial viscous cell center, the lobe cell center, and the nightside edge of the lobe cell. Data points for $D \geq 0$ were determined from the dawnside simulation results, assuming the rotational symmetry. The line for the topological cusp is shown dotted for clarity. We

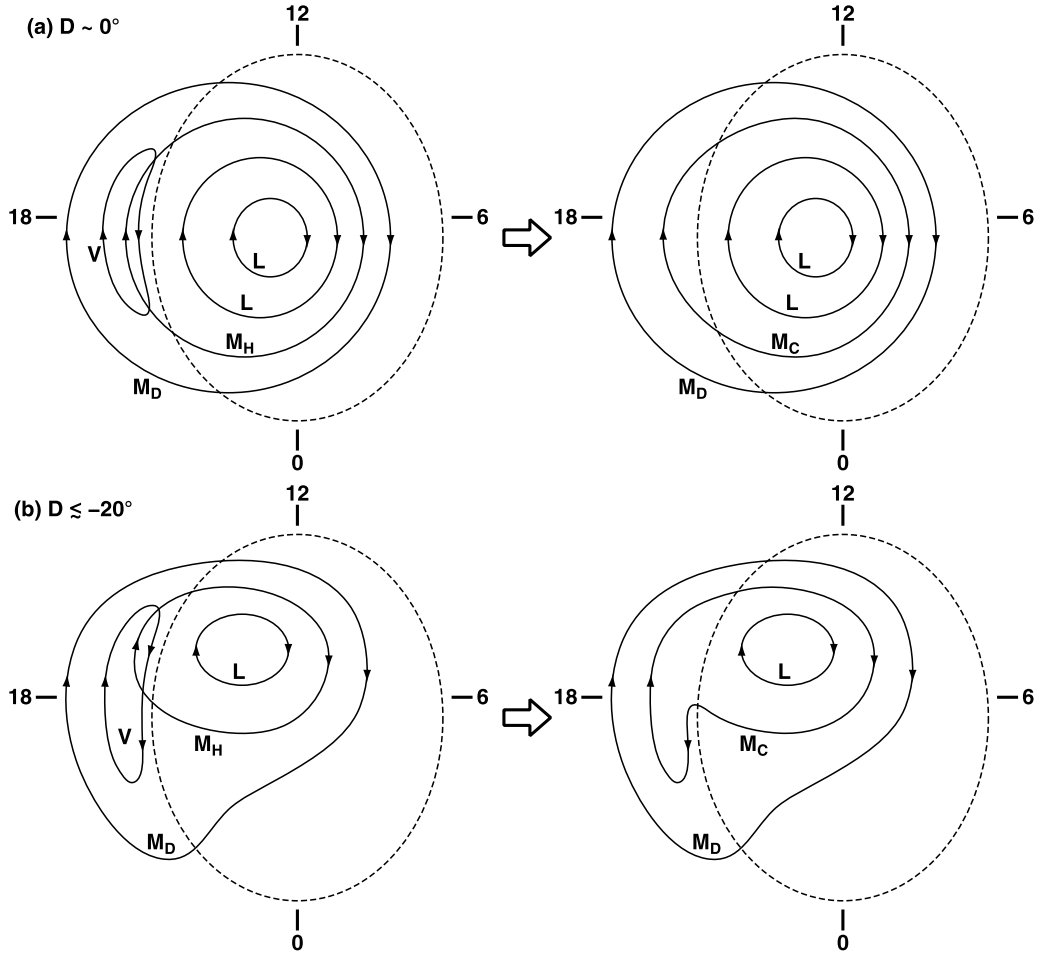

Figure 13. Schematics showing how the lobe cell position relative to the viscous cell changes the convection pattern in the round cell hemisphere for (a) the $D \sim 0°$ case and (b) the $D \lesssim -20°$ case. Convection cells are denoted by L (lobe cell), M_D (Dungey-type merging cell), M_H (hybrid merging cell), V (viscous cell), and M_C (coalescent merging cell). Each streamline is assumed to represent a potential drop of Φ.

see that the S value of the sunward edge of the polar cap remains almost constant irrespective of the dipole tilt, which indicates the utility of describing the position of an ionospheric point by this coordinate. The topological cusp moves antisunward with increasing D as expected from the vacuum superposition model, but the magnitude of the displacement is only a few degrees. The sunward edge of the lobe cell shows nearly the same values as the topological cusp, which is useful information for estimating practically the topological cusp location from observational data. The viscous cell center also moves antisunward with increasing D, but the antisunward shift is only a few degrees and almost parallel to the antisunward shift of the topological cusp. The viscous cell center is always located antisunward of the topological cusp, which is probably related to the antisunward shift of the potential peak on the round-cell-side polar cap boundary, as discussed in section 4.2.

[40] We now examine the relative position of the viscous cell and the lobe cell as originally intended. The lobe cell center and the sunward edge of the lobe cell moves antisunward with increasing D, but the relative position of these points with respect to the projected viscous cell center does not change drastically with D. What does change significantly with respect to the viscous cell center is the nightside edge of the lobe cell for $D \leq 0$. While, for $D \lesssim -20°$, the lobe cell on the dayside is confined to a region closer to the projected viscous cell center, the lobe cell expands to the nightside for $D \sim 0°$. This expansion would be due not only to the geometry change with the dipole tilt change but also to the intensity change of the lobe cell. As Figure 10 shows, the lobe cell potential becomes very weak for $D \lesssim -20°$.

4.4. Round Cell Geometry

[41] Our goal is to explain the deformation of the round cell in the winter hemisphere. As noted in section 2, the round cell in Figures 2c and 2e is not really round but has a "tadpole tail" extending to the premidnight sector. It is expected that the deformed merging cell streamlines are a "fossil" of the viscous cell. We suggest that two factors are responsible for this round cell deformation. One factor is the intensity of the viscous cell. When the viscous cell moves toward the Sun owing to the dipole tilt, the viscous cell intensity tends to increase (section 4.2). The other factor is the relative position of the viscous cell and the hybrid merging cell. The lobe cell (whose extent represents the inner edge of the hybrid merging

cell) expands to the nightside in spring, fall, and summer but is confined to the dayside in winter (section 4.3).

[42] Figure 13 illustrates how the lobe cell position relative to the viscous cell affects the shape of the coalescent merging cell, with Figure 13a showing the $D \sim 0°$ case and Figure 13b showing the $D \lesssim -20°$ case. In order to emphasize the lobe cell potential difference between the two cases, two lobe cell streamlines are drawn for the former case. We assume that the diffusion effect is minimal so that a hybrid merging cell (M_H) and a viscous cell (V), each having the same potential Φ, are incorporated into a coalescent merging cell (M_C) with a potential drop of Φ. For $D \sim 0°$, the lobe cell extends to the nightside polar cap, and consequently so does the hybrid merging cell. When the viscous cell is incorporated into the hybrid merging cell, the resultant coalescent merging cell is still round (Figure 13a). In contrast, for $D \lesssim -20°$, the lobe cell is confined to the dayside polar cap, and consequently so is the hybrid merging cell. Because of this shrinking, the coalescent merging cell has a tadpole-tail-like protrusion which is regarded as a "fossil" of the viscous cell (Figure 13b). In addition, the duskside viscous cell intensity is larger for $D \lesssim -20°$ than for $D \sim 0°$. We suggest that the synergetic effect of the two factors − (1) the relative position of the hybrid merging and viscous cells and (2) the intensity of the viscous cell – produces the difference between Figure 2a (round merging cell) and Figures 2c and 2e (tadpole-shaped merging cell).

5. Conclusions

[43] Using numerical MHD simulations, we examined the effect of dipole tilt on the magnetosphere-ionosphere convection system for IMF $B_Y > 0$ (IMF clock angle $\theta_c = 63°$). The dipole tilt is parameterized by the angle D between the GSM Z axis and the SM Z axis (D is positive for boreal summer).

[44] In our simulation, both reconnection-driven convection and "viscous-driven" convection play important roles in the global magnetic flux circulation. When there is no dipole tilt ($D = 0°$), the viscous cell centers in the GSM equatorial plane are located approximately at dawn and dusk. The azimuthal locations of the viscous cells rotate clockwise (counterclockwise) in the GSM X-Y plane when D decreases from 0° to −35° (when D increases from 0° to +35°). We found that this rotation is related to the geometry of the dayside separator. The equatorial crossing point of the dayside separator exhibits the same rotation in the GSM X-Y plane as the viscous cell centers. This is because the viscous circulation is formed inside the Dungey circulation which, in turn, is geometrically constrained by the separatrix shape. The separators demarcate the dawnside Dungey circulation and the duskside Dungey circulation, and the demarcation in the equatorial plane is determined by the equatorial crossing point of the dayside separator.

[45] The convection in the ionosphere is basically the round/crescent cell pattern, but this basic pattern is affected by the presence of the viscous cell. In the crescent cell hemisphere, the viscous cell is naturally embedded in the reconnection-driven merging cell to form a crescent cell, but in the round cell hemisphere, the antisunward convection in the poleward part of the viscous cell is canceled by the sunward flow of the hybrid merging cell, resulting in formation of one round merging cell. When the dipole tilt is significant ($|D| \gtrsim 20°$), the round cell in the winter hemisphere is associated with a "fossil" of the viscous cell. We suggest that two factors are affecting the round cell deformation. One is the viscous cell intensity, and the other is the extent of the lobe cell that is embedded in the hybrid merging cell. The duskside (dawnside) viscous cell tends to intensify for $D \lesssim -20°$ ($D \gtrsim 20°$) compared to $D \sim 0°$. The lobe cell (and consequently the encompassing hybrid merging cell) in the winter hemisphere is confined on the dayside for $|D| \lesssim 20°$, whereas it extends to the nightside polar cap for $D \sim 0°$.

[46] The numerical and conceptual modeling in this paper provides a framework for interpreting observations. In fact, the round cell deformation discussed in Figure 13b is similar to the observed convection pattern in Figure 1. However, in observations, the round cell "splits" into two. It is somewhat doubtful that the splitting arises because the viscous cell potential becomes larger than the hybrid merging cell potential. Detailed analysis of the observational data and comparison with the simulations will be required in the future.

[47] **Acknowledgments.** M. Watanabe was funded by a Canadian Space Agency (CSA) Space Science Enhancement Program grant, a Natural Sciences and Engineering Research Council (NSERC) Canada Collaborative Research Opportunities Grant for the e-POP satellite mission, and a CSA contract for the e-POP mission. The motivation for the research is an understanding of the convection patterns measured both by the Canadian SuperDARN radars (operated with funding from both an NSERC Major Resource Support Grant and a CSA contract) and by the international SuperDARN radars funded by a number of national funding agencies.

[48] Wolfgang Baumjohann thanks Nancy Crooker and another reviewer for their assistance in evaluating this paper.

References

Alekseyev, I. I., and Y. S. Belen'kaya (1983), Electric field in an open model of the magnetosphere, *Geomagn. Aeron.*, *23*, 57–61.

Axford, W. I., and C. O. Hines (1961), A unifying theory of high-latitude geophysical phenomena and geomagnetic storms, *Can. J. Phys.*, *39*, 1433–1464.

Burch, J. L., P. H. Reiff, J. D. Menietti, R. A. Heelis, W. B. Hanson, S. D. Shawhan, E. G. Shelley, M. Sugiura, D. R. Weimer, and J. D. Winningham (1985), IMF B_Y-dependent plasma flow and Birkeland currents in the dayside magnetosphere: 1. Dynamics Explorer observations, *J. Geophys. Res.*, *90*(A2), 1577–1593, doi:10.1029/JA090iA02p01577.

Crooker, N. U. (1992), Reverse convection, *J. Geophys. Res.*, *97*(A12), 19,363–19,372, doi:10.1029/92JA01532.

Crooker, N. U., J. G. Lyon, and J. A. Fedder (1998), MHD model merging with IMF B_Y: Lobe cells, sunward polar cap convection, and overdraped lobes, *J. Geophys. Res.*, *103*(A5), 9143–9151, doi:10.1029/97JA03393.

Dorelli, J. C., A. Bhattacharjee, and J. Raeder (2007), Separator reconnection at Earth's dayside magnetopause under generic northward interplanetary magnetic field conditions, *J. Geophys. Res.*, *112*, A02202, doi:10.1029/2006JA011877.

Dungey, J. W. (1961), Interplanetary magnetic field and the auroral zones, *Phys. Rev. Lett.*, *6*, 47–48, doi:10.1103/PhysRevLett.6.47.

Greene, J. M. (1992), Locating three-dimensional roots by a bisection method, *J. Comput. Phys.*, *98*(2), 194–198, doi:10.1016/0021-9991(92)90137-N.

Kivelson, M. G., and C. T. Russell (1995), Introduction to Space Physics, 568 pp., Cambridge Univ. Press, New York.

Lu, G., et al. (1994), Interhemispheric asymmetry of the high-latitude ionospheric convection pattern, *J. Geophys. Res.*, *99*(A4), 6491–6510, doi:10.1029/93JA03441.

Parker, E. N. (1996), The alternative paradigm for magnetospheric physics, *J. Geophys. Res.*, *101*(A5), 10,587–10,625, doi:10.1029/95JA02866.

Powell, K. G., P. L. Roe, T. J. Linde, T. I. Gombosi, and D. L. DeZeeuw (1999), A solution-adaptive upwind scheme for ideal magnetohydrodynamics, *J. Comput. Phys.*, *154*(2), 284–309, doi:10.1006/jcph.1999.6299.

Reiff, P. H., and J. L. Burch (1985), IMF B_Y-dependent plasma flow and Birkeland currents in the dayside magnetosphere: 2. A global model for northward and southward IMF, *J. Geophys. Res.*, *90*(A2), 1595–1609, doi:10.1029/JA090iA02p01595.

Ridley, A. J., T. I. Gombosi, and D. L. DeZeeuw (2004), Ionospheric control of the magnetosphere: Conductance, *Ann. Geophys.*, *22*, 567–584.

Russell, C. T. (1972), The configuration of the magnetosphere, in *Critical Problems of Magnetospheric Physics*, edited by E. R. Dyer, pp. 1–16, Natl. Acad. of Sci., Washington, D. C.

Schindler, K., M. Hesse, and J. Birn (1988), General magnetic reconnection, parallel electric fields, and helicity, *J. Geophys. Res.*, *93*(A6), 5547–5557, doi:10.1029/JA093iA06p05547.

Siscoe, G. L. (1988), The magnetospheric boundary, in *Physics of Space Plasmas (1987)*, edited by T. Chang, G. B. Crew, and J. R. Jasperse, pp. 3–78, Sci. Publ., Cambridge, Mass.

Siscoe, G. L., G. M. Erickson, B. U. Ö. Sonnerup, N. C. Maynard, K. D. Siebert, D. R. Weimer, and W. W. White (2001a), Magnetospheric sash dependence on IMF direction, *Geophys. Res. Lett.*, *28*(10), 1921–1924, doi:10.1029/2000GL003784.

Siscoe, G. L., G. M. Erickson, B. U. Ö. Sonnerup, N. C. Maynard, K. D. Siebert, D. R. Weimer, and W. W. White (2001b), Global role of $E_{\|}$ in magnetopause reconnection: An explicit demonstration, *J. Geophys. Res.*, *106*(A7), 13,015–13,022, doi:10.1029/2000JA000062.

Tanaka, T. (1999), Configuration of the magnetosphere-ionosphere convection system under northward IMF conditions with nonzero IMF B_Y, *J. Geophys. Res.*, *104*(A7), 14,683–14,690, doi:10.1029/1999JA900077.

Tanaka, T. (2007), Magnetosphere-ionosphere convection as a compound system, *Space Sci. Rev.*, *133*(1–4), 1–72, doi:10.1007/s11214-007-9168-4.

Vasyliūnas, V. M. (2001), Electric field and plasma flow: What drives what?, *Geophys. Res. Lett.*, *28*(11), 2177–2180, doi:10.1029/2001GL013014.

Vasyliūnas, V. M. (2005a), Time evolution of electric fields and currents and the generalized Ohm's law, *Ann. Geophys.*, *23*, 1347–1354.

Vasyliūnas, V. M. (2005b), Relation between magnetic fields and electric currents in plasmas, *Ann. Geophys.*, *23*, 2589–2597.

Watanabe, M., and G. J. Sofko (2008), Synthesis of various ionospheric convection patterns for IMF B_Y-dominated periods: Split crescent cells, exchange cells, and theta aurora formation, *J. Geophys. Res.*, *113*, A09218, doi:10.1029/2007JA012868.

Watanabe, M., and G. J. Sofko (2009a), Role of interchange reconnection in convection at small interplanetary magnetic field clock angles and in transpolar arc motion, *J. Geophys. Res.*, *114*, A01209, doi:10.1029/2008JA013426.

Watanabe, M., and G. J. Sofko (2009b), The interchange cycle: A fundamental mode of magnetic flux circulation for northward interplanetary magnetic field, *Geophys. Res. Lett.*, *36*, L03107, doi:10.1029/2008GL036682.

Watanabe, M., and G. J. Sofko (2009c), Dayside four-sheet field-aligned current system during IMF B_Y-dominated periods, *J. Geophys. Res.*, *114*, A03208, doi:10.1029/2008JA013815.

Watanabe, M., G. J. Sofko, D. A. André, T. Tanaka, and M. R. Hairston (2004), Polar cap bifurcation during steady-state northward interplanetary magnetic field with $|B_Y| \sim B_Z$, *J. Geophys. Res.*, *109*, A01215, doi:10.1029/2003JA009944.

Watanabe, M., K. Kabin, G. J. Sofko, R. Rankin, T. I. Gombosi, A. J. Ridley, and C. R. Clauer (2005), Internal reconnection for northward interplanetary magnetic field, *J. Geophys. Res.*, *110*, A06210, doi:10.1029/2004JA010832.

Watanabe, M., G. J. Sofko, K. Kabin, R. Rankin, A. J. Ridley, C. R. Clauer, and T. I. Gombosi (2007), Origin of the interhemispheric potential mismatch of merging cells for interplanetary magnetic field B_Y-dominated periods, *J. Geophys. Res.*, *112*, A10205, doi:10.1029/2006JA012179.

White, W. W., G. L. Siscoe, G. M. Erickson, Z. Kaymaz, N. C. Maynard, K. D. Siebert, B. U. Ö. Sonnerup, and D. R. Weimer (1998), The magnetospheric sash and the cross-tail S, *Geophys. Res. Lett.*, *25*(10), 1605–1608, doi:10.1029/98GL50865.

Yeh, T. (1976), Day side reconnection between a dipolar geomagnetic field and a uniform interplanetary field, *J. Geophys. Res.*, *81*(13), 2140–2144, doi:10.1029/JA081i013p02140.

T. I. Gombosi and A. J. Ridley, Department of Atmospheric, Oceanic, and Space Sciences, University of Michigan, Ann Arbor, MI 48109, USA.

K. Kabin and R. Rankin, Department of Physics, University of Alberta, Edmonton, AB T6G 2M7, Canada.

G. J. Sofko, Department of Physics and Engineering Physics, University of Saskatchewan, Saskatoon, SK S7N 5E2, Canada.

M. Watanabe, Department of Earth and Planetary Sciences, Graduate School of Sciences, Kyushu University, 6-10-1 Hakozaki, Higashi-ku, Fukuoka 812-8581, Japan. (watanabe.masakazu.852@m.kyushu-u.ac.jp)